ARTICLE

Check for updates

Destabilization of spin-Peierls phase via a charge-spin modulated Floquet state induced by intramolecular vibrational excitation

Daiki Sakai[1,2], Takashi Yamakawa [1,2], Hajime Ueda[1], Ryohei Ikeda[1], Tatsuya Miyamoto [1✉] & Hiroshi Okamoto [1✉]

The electronic state control using a periodic light field is one of the central subjects in photophysics. In molecular solids, intramolecular vibrations sometimes couple to inter-molecular electron transfer, thus modulating electron and spin densities of each molecule. Here, we show that in a quasi-one-dimensional molecular solid K-tetracyanoquinodimethane (TCNQ) in which TCNQ molecules are dimerized by the spin-Peierls mechanism, an intra-molecular vibrational excitation with a phase-locked mid-infrared pulse induces a charge-spin modulated Floquet state, which destabilizes the spin-Peierls phase. By detecting reflectivity changes of the intramolecular transition band along the mid-infrared electric field with 6.6-fs probe pulses, we detected high-frequency oscillations reflecting electron- and spin-density modulations synchronized with intramolecular vibrations. More significantly, we observed an oscillation of ~110 cm^{-1} due to a dimeric mode driven by a decrease in spin-Peierls dimer-ization. This dimerization reduction was confirmed by measuring transient reflectivity changes of the Mott-gap transition band. These results demonstrate the effectiveness of intramolecular vibrational excitation as a method for Floquet engineering in molecular solids.

---

[1] Department of Advanced Materials Science, University of Tokyo, Chiba 277-8561, Japan. [2] These authors contributed equally: Daiki Sakai, Takashi Yamakawa. ✉email: miyamoto@k.u-tokyo.ac.jp; okamotoh@k.u-tokyo.ac.jp

Photoinduced phase transitions of correlated electron systems, in which electronic and crystal structures are changed by irradiating solids with a femtosecond laser pulse, have been actively investigated[1–3]. The dynamics of nonequilibrium excited states can provide insights into the interplay in electron, spin, and lattice systems, which cannot be obtained via steady-state measurements. In most studies, visible pulses beyond the optical gap have been used for excitations[4–17]. In these investigations, photoexcitation-induced interband transitions or intermolecular electron transfers caused macroscopic electronic-state changes via strong electron-electron, electron-lattice, and spin-lattice interactions. However, their dynamics are complicated because high-energy electronic excited states induce large temperature increases in systems during their relaxation processes.

Recently, electronic-state controls using a mid-infrared (MIR) pulse have attracted attention as an approach for addressing the drawbacks of visible-pulse excitations[18–29]. Using an MIR pulse, it is possible to generate a strong electric field of the order of 10 MV cm^{-1}, which can induce nonperturbative responses such as quantum tunneling processes[30,31]. If molecular or lattice vibrations that interact strongly with an electronic system are resonantly excited using an MIR pulse, periodic charge or spin modulation can be induced[19–22,24,26–28]. This can facilitate efficient electronic- and spin-state control, which is called Floquet engineering[32–39]. Although studies on vibrational excitations have been reported from this perspective, for example, the observation of high order phonon harmonics in LiNbO$_3$ (ref. [24]), modulation of on-site Coulomb repulsion[19,20], observation of light-induced superconductivity[21], and observation of phonon-dressed Floquet states in molecular solids[28], there are limited examples of electronic-phase control in solids.

Here, we focus on the control of electron and spin states in molecular solids using vibrational excitations. Figure 1a shows a schematic of a dimer of molecules with singly occupied molecular orbitals (SOMO) and totally symmetric intramolecular vibration (a_g mode) (blue open arrows). The a_g mode is not IR-active in isolated molecules. However, given that it modulates the SOMO energy up and down, an out-of-phase a_g-mode vibration in a dimer induces intermolecular electron transfer that is synchronized with the vibration and becomes IR-active for an electric field E along the direction of molecular stacking[40]. Such an interaction between electrons and the a_g mode vibrations is called

electron-intramolecular-vibration (EMV) coupling. Thus, the excitation of the IR-active a_g mode can give rise to coherent electron- and spin-density oscillations in each dimer, which corresponds to a generation of a charge-spin modulated Floquet state.

To induce an electronic-state change using this type of Floquet state, we chose a spin-Peierls system of potassium-tetracyanoquinodimethane (K-TCNQ). Figure 1b shows the crystal structure of K-TCNQ. In this compound, an electron is transferred from K to TCNQ, and each TCNQ$^-$ has a SOMO. TCNQ$^-$ molecules are stacked along the a-axis, forming a half-filled one-dimensional electronic system owing to the molecular orbital overlap between neighboring molecules[41]. The on-site Coulomb repulsion U (~1.5 eV) of TCNQ is large relative to the intermolecular transfer integral t_0 (~0.2 eV), thus, the system is a Mott insulator[42–44]. The electron spin ($S = 1/2$) on TCNQ$^-$ forms an antiferromagnetic chain (red arrows in Fig. 1c). Below the critical temperature $T_c = 395$ K, molecules dimerize to form a spin singlet state in each dimer (Fig. 1d), which is called a spin-Peierls transition[41,45]. A previous study revealed that visible femtosecond-pulse irradiation destabilized the spin-Peierls phase and decreased molecular dimerization[8,46]. The electron carriers (doublons) and hole carriers (holons) generated by the photo-excitation do not have spin and thus breaks up the anti-ferromagnetic spin chain. It was suggested that the fragment of spin chains resulted in the suppression of the spin-Peierls mechanism and reduction in the dimer molecular displacements[8,46]. The excitation of the a_g-mode vibrations with EMV couplings (Fig. 1a) by an MIR pulse should induce the spin-density modulation as well as the charge-density one. The spin-density modulation is expected to destabilize the spin-Peierls phase since it hybridizes the antiferromagnetic ground state with the non-magnetic state.

In this study, we detected the ultrafast dynamics in the destabilization of the spin-Peierls phase via the formation of the charge-spin modulated Floquet state by a subcycle spectroscopy using a phase-locked MIR pump pulse and an ultrashort visible probe pulse. The analyses of the reflectivity changes in the intramolecular transition band revealed that the electron and spin density of each molecule are synchronously modulated with intramolecular vibrations. Additionally, we demonstrated that such a charge-spin modulation induces dimerization reduction, as
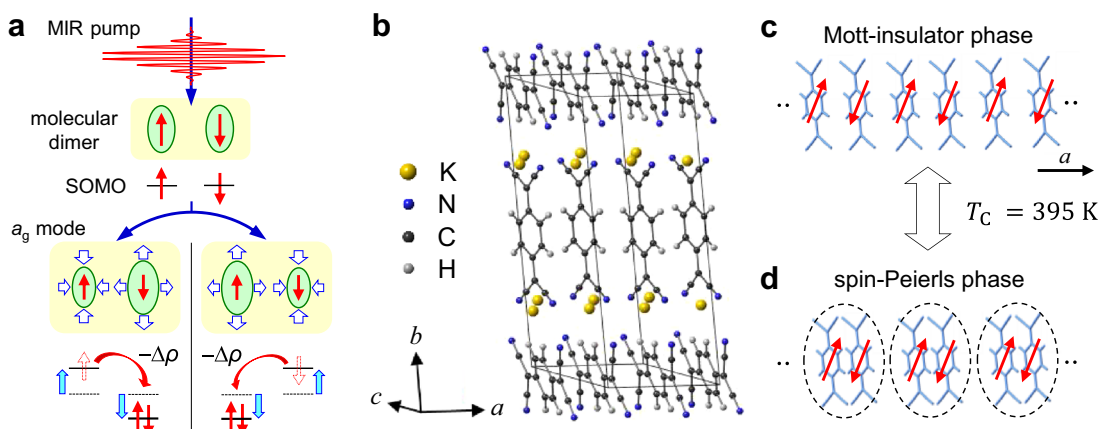
Fig. 1 Charge and spin modulation by an intramolecular vibrational excitation with a mid-infrared (MIR) pulse in a spin-Peierls system of K-tetracyanoquinodimethane (TCNQ). a Schematic of an out-of-phase totally symmetric intramolecular vibration (a_g mode) (blue open arrows) in a molecular dimer with one electron in each molecular orbital, which can be excited by an MIR pulse. Energy modulations of two singly occupied molecular orbitals (SOMO) coupled with a_g-mode vibrations induce partial charge transfers, $\Delta\rho$, in a molecular dimer, resulting in spin-density modulations in each molecule as shown in the lower part. **b** The crystal structure of K-TCNQ. The thin lines represent unit cell. **c**, **d** Schematics of **c** Mott-insulator phase and **d** spin-Peierls phase with molecular dimerizations in K-TCNQ. $T_C = 395$ K is the critical temperature.

observed in transient reflectivity changes of the Mott-gap transition band. This approach using an intramolecular vibrational excitation is an example of Floquet engineering and can be applied to drive various phase transitions in other molecular solids with strong electron-phonon couplings.

Results

Steady-state polarized reflectivity spectra. Figure 2a shows the polarized reflectivity (R) spectra on the ab plane. The broad peak at 1 eV for the electric field of light E parallel to the a axis ($E//a$) corresponds to the Mott-gap transition (orange arrow in the inset)[43,44]. The sharp peaks below 0.3 eV are the aforementioned a_g-mode vibrations of TCNQ$^-$ (refs. [47,48]). The atomic motions in TCNQ in mode 1 with $\Omega_1 = 1178$ cm^{-1} and mode 2 with $\Omega_2 = 1330$ cm^{-1} are illustrated in the inset[28,47]. The band at 2 eV for E perpendicular to the a axis ($E \perp a$) is the intramolecular transition (IMT) from the highest occupied molecular orbital of TCNQ$^-$ to SOMO (blue arrow in the inset)[43,44,49]. The intensity of this transition is sensitive to the electron and spin densities of the SOMO.

MIR pump ultrashort visible reflectivity probe subcycle measurements on the intramolecular transition band. Figure 2b illustrates a schematic of the MIR pump subcycle reflection probe spectroscopy, which is almost identical to that used in a previous study, in which Floquet states concerning the intramolecular excited state were detected[28]. In the present study, we focus on the electronic-state control by generating Floquet states of the ground state, in which the nonmagnetic states are mixed with the original spin singlet states. The electric-field waveform and Fourier power spectrum of the MIR pulse are shown in Figs. 3a and 2a, respectively. This pulse has a central frequency of 1069 cm^{-1}, exciting mode 1 strongly and mode 2 weakly. Figure 2c shows a temporal profile of the ultrashort visible probe pulse. This pulse has a temporal width δt_r of 6.6 fs ($E \perp a$), which is sufficiently shorter than the period of the MIR pulse, ~30 fs, enabling subcycle spectroscopy. Its spectrum shown in Fig. 2a (the blue shade) covers the IMT of TCNQ$^-$, which facilitates the detection of changes in the electron and spin densities of each molecule via its reflectivity change, $\Delta R(t)/R$, where t is the delay time of the probe pulse relative to the MIR-pump pulse. A bandpass filter with a bandwidth of ~35 meV and a central photon energy of 2.07 eV

was inserted in front of the detector to measure $\Delta R(t)/R$ at the IMT peak. Technical details of the experiments can be found in the Methods section and Supplementary Note 1. The selection of the probe energy is detailed in Supplementary Note 2. All measurements were performed at 294 K.

Figure 3b shows the time evolution of the reflectivity changes, $\Delta R(t)/R$, for the MIR pulse with the maximum electric-field amplitude, E_{MIR}, of 2.1, 4.1 and 6.1 MV cm^{-1}. $\Delta R(t)/R$ exhibits high-frequency oscillations with a period of ~14 fs, which is almost half the MIR-light period. The thick lines show the low-frequency component below 10 THz, $\Delta R_{LF}(t)/R$, which was extracted using a Fourier filter. In $\Delta R_{LF}(t)/R$, low-frequency oscillations with a period of ~200 fs or more and a long-lived decrease in the reflectivity were observed. The high and low frequency oscillations are expected to be related to the out-of-phase a_g-mode vibration and lattice-mode vibrations due to the destabilization of the spin-Peierls phase, respectively.

First, to clarify the origin of the high-frequency oscillations, we extracted the high-frequency components $\Delta R_{HF}(t)/R$ above 20 THz from $\Delta R(t)/R$ for $E_{MIR} = 6.1$ MV cm^{-1}, using a Fourier filter. The extracted profile of $\Delta R(t)/R$ is shown by the open circles in Fig. 4b. The Fourier power spectrum of $\Delta R_{HF}(t)/R$, I_{HF}, is shown in Fig. 3d, in which a strong peak at ~2370 cm^{-1} and weak peaks at ~2210 and ~2530 cm^{-1} were identified. The spectral shapes of I_{HF} for $E_{MIR} = 2.1$ MV cm^{-1} and 4.1 MV cm^{-1} are almost identical with that for $E_{MIR} = 6.1$ MV cm^{-1}. To elucidate the origins of these oscillations, we show the ε_2 spectra of modes 1,2 obtained from the R spectrum using the Kramers-Kronig transform in Fig. 3c and the Raman spectrum in the $z(xx)\bar{z}$ configuration in Fig. 3e (see the Methods section for the details of the steady-state optical spectroscopy measurements). The horizontal scale in Fig. 3c is half of that in Figs. 3d and 3e. x and z correspond to the a-axis and normal to the ab-plane, respectively. The peak frequencies of ~2370 cm^{-1} and ~2530 cm^{-1} in I_{HF} almost coincide with $2\Omega_1 = 2356$ cm^{-1} and $\Omega_1 + \Omega_2 = 2508$ cm^{-1}, respectively, where $\Omega_1 = 1178$ cm^{-1} and $\Omega_2 = 1330$ cm^{-1} are the frequencies of mode 1 and mode 2, respectively (Fig. 3c). Therefore, these oscillations correspond to the charge modulation in each dimer by a_g modes via EMV coupling (Fig. 1a). The modulation of the SOMO energy ϵ_s in each molecule can be written as $\epsilon_s \propto [g_1 Q_1(t) + g_2 Q_2(t)]$, where $Q_i(t)$ and g_i ($i = 1,2$) show the normal coordinate and EMV-coupling constant of each mode, respectively[40]. g_i is a parameter
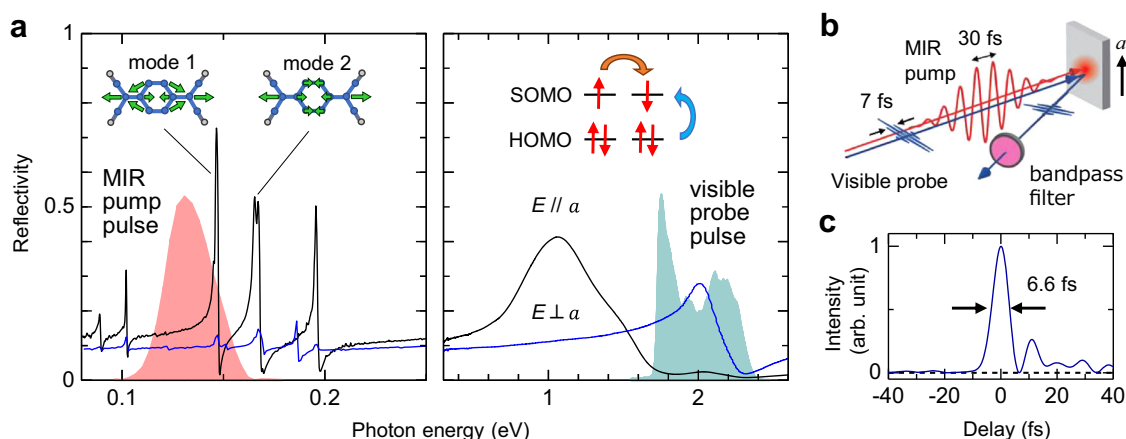
Fig. 2 Experimental condition of mid-infrared (MIR)-pump visible reflectivity probe subcycle measurements. a Polarized reflectivity spectra of K-tetracyanoquinodimethane (TCNQ) at 294 K. The black and blue solid lines are for the electric field of light E parallel and perpendicular to the a axis ($E//a$ and $E \perp a$), respectively. The red and blue shades show the spectra of MIR-pump and visible-probe pulses, respectively. The inset in the right panel illustrates the Mott-gap transition (the orange arrow) and intramolecular transition (IMT) (the blue arrow). The inset in the left panel illustrates the atomic motions of modes 1 and 2. SOMO and HOMO represent the singly and highest occupied molecular orbitals, respectively. **b** Schematic of the experimental setup. **c** The intensity envelope of the ultrashort visible probe pulse.
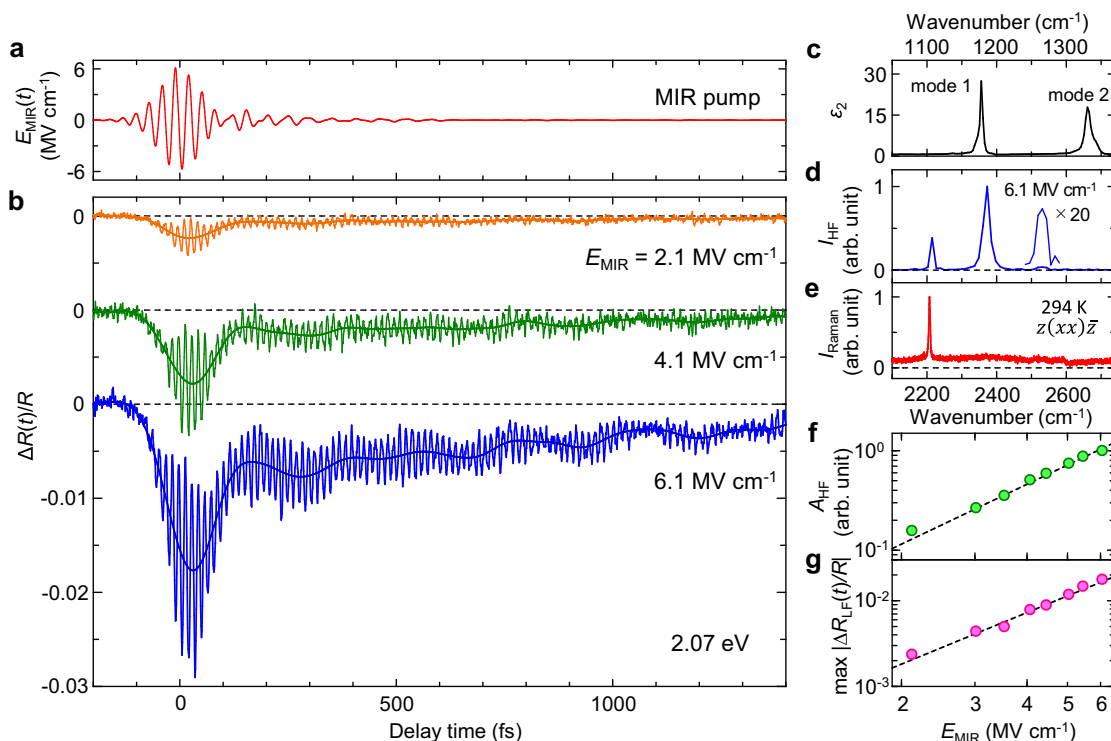
Fig. 3 Reflectivity changes in the intramolecular transition band induced by the phase-locked mid-infrared (MIR) pump pulse. a Electric-field waveform, $E_{MIR}(t)$, of the MIR pulse. **b** Time characteristics of the reflectivity change $\Delta R(t)/R$ at 2.07 eV at 294 K (the thin solid lines). The thick solid lines show the low-frequency components below 10 THz, $\Delta R_{LF}(t)/R$. The orange, green and blue solid lines are for the MIR pulse with the maximum electric-field amplitude, E_{MIR}, of 2.1, 4.1 and 6.1 MV cm^{-1}, respectively. **c** Imaginary part of the dielectric constant (ε_2) spectrum for the electric field of light E parallel to the a axis ($E//a$) at 294 K. **d** Fourier power spectrum, I_{HF}, of the high-frequency components $\Delta R_{HF}(t)/R$ in the temporal range from 200 fs to 2950 fs. **e** Raman spectrum, I_{Raman}, for $z(xx)\bar{z}$ configuration at 294 K. x and z correspond to the a-axis and the normal to the ab-plane, respectively. **f** E_{MIR}-dependence of amplitudes of the high-frequency components A_{HF} of $2\Omega_1$-oscillation. **g** E_{MIR}-dependence of max$|\Delta R_{LF}(t)/R|$ around the time origin. Broken lines in **f**, **g** are proportional to $(E_{MIR})^2$. The error bars are smaller than the sizes of data points.
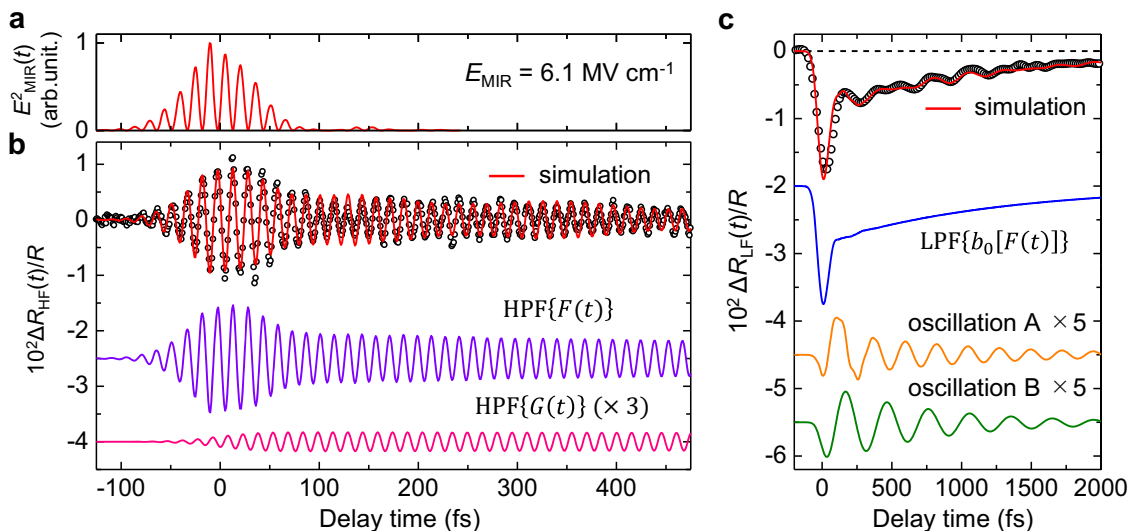
Fig. 4 Fitting analyses of high- and low- frequency components of reflectivity changes. a The square of the electric-field waveform $E_{MIR}(t)$ of the mid-infrared (MIR) pulse with the maximum electric-field amplitude, E_{MIR}, of 6.1 MV cm^{-1}. **b** Time characteristics of the high-frequency component $\Delta R_{HF}(t)/R$ (open circles). The red line shows the fitting curves. The purple and pink solid lines represent the components of the fitting curve corresponding to HPF{$F(t)$} and HPF{$G(t)$} in Eq. (1), respectively. HPF is an operator that extracts high-frequency components. $F(t)$ and $G(t)$ are functions defined by Eq. (2) and Eq. (3), respectively. **c** Time characteristics of the low-frequency components $\Delta R_{LF}(t)/R$(open circles) and the fitting curves (red line). The blue, orange and green solid lines represent the components of the fitting curve corresponding to the first, the third, and the second terms (LPF{$b_0[F(t)]$}, oscillation A, and oscillation B) in Eq. (6), respectively. LPF shows an operator that extracts a low-frequency component.

that characterizes how much the SOMO energy changes with the intramolecular vibration $Q_i(t)$ and is defined by $g_i = \sqrt{\frac{\hbar}{\Omega_i}} \frac{\partial \epsilon_s}{\partial Q_i}$. Since K-TCNQ has inversion symmetry, the reflectivity change is proportional to $[g_1 Q_1(t) + g_2 Q_2(t)]^2$, which should include oscillatory components with the frequencies of $2\Omega_1$, $2\Omega_2$, $\Omega_1 + \Omega_2$, $\Omega_1 - \Omega_2$. Since mode 2 with the frequency Ω_2 was not strongly excited as compared to mode 1 with the frequency Ω_1 in the experiment as mentioned above, the oscillation of $(\Omega_1 + \Omega_2)$ is much weaker than that of $2\Omega_1$, and the oscillation of $2\Omega_2$ is not observed. $Q_1(t)$ and $Q_2(t)$ are proportional to E_{MIR}. Therefore, the amplitudes of the observed oscillations, A_{HF}, are expected to be proportional to $(E_{MIR})^2$. In fact, the magnitudes of A_{HF} of the oscillation with the frequency of $2\Omega_1$ evaluated from the Fourier power spectra exhibits a $(E_{MIR})^2$ dependence as shown in Fig. 3f.

On the other hand, the oscillation at 2210 cm^{-1} corresponds to no peak in the ϵ_2 spectrum, but to the peak ($\sim$2200 cm^{-1}) seen in the Raman spectrum in Fig. 3e. Therefore, this oscillation is attributable to the Raman mode excited by a two-photon process[23]. In this mode, all the molecules vibrate in phase and no intermolecular charge transfers are induced. Furthermore, the MIR electric field, $E_{MIR}(t)$, is expected to induce charge modulation directly in non-resonant and coherent manner. The reflectivity change due to this modulation should occur during the presence of the pump pulse and be proportional to $E_{MIR}(t)^2$.

Considering these facts, we performed a fitting analysis of the high-frequency component above 20 THz ($\Delta R_{HF}(t)/R$) using the following equations, in which the weak 2530 cm^{-1} oscillation was neglected.

$$\frac{\Delta R_{HF}(t)}{R} = HPF\{F(t) + G(t)\} \tag{1}$$

$$F(t) = \{a_0 E_{MIR}(t) + a_1[E_{MIR}(t) \otimes f_1(t)]\}^2 \tag{2}$$

$$G(t) = a_3{}^2 [E_{MIR}(t)]^2 \otimes f_3(t) \tag{3}$$

$$f_i(t) = \exp\left(-\frac{t}{\tau_i}\right) \sin(\omega_i t + \phi_i) \quad (i = 1, 3) \tag{4}$$

$$g(t) \otimes f_i(t) = \int_{-\infty}^{t} g(\tau) f_i(t - \tau) d\tau \tag{5}$$

Here, HPF in Eq. (1) is an operator that extracts high-frequency components. $a_0 E_{MIR}(t)$ on the right-hand side of Eq. (2) represents the direct charge modulation by the MIR electric field $E_{MIR}(t)$. The next term, $a_1[E_{MIR}(t) \otimes f_1(t)]$, represents the charge modulation due to the a_g-mode vibration (mode 1) driven by the MIR electric field $E_{MIR}(t)$ via the EMV coupling. $f_1(t)$ in Eq. (2) is a damped oscillator for mode 1. ω_1, ϕ_1, and τ_1 are the frequency, initial phase, and decay time of the mode-1 vibration. $\otimes$ shows a convolution integral, the definition of which is shown in Eq. (5), where $g(t)$ shows a driving force of oscillator $f_i(t)$. a_0 and a_1 are the parameters determining the magnitude of each term. The time dependence of the a_g-mode vibration of each molecule in a dimer is expressed using the convolution integral of $f_1(t)$ with $E_{MIR}(t)$ as shown in Eq. (2). The reflectivity change due to the direct charge modulation by the MIR electric field and the charge modulation by the out-of-phase a_g-mode vibration in each dimer is expressed

by the high-frequency component of square of $\{a_0 E_{MIR}(t) + a_1[E_{MIR}(t) \otimes f_1(t)]\}$, as shown in Eq. (2). $G(t)$ in Eq. (3) expresses the reflectivity change due to the Raman-active a_g mode excited by the two-photon absorption process of the MIR pulse. This Raman-active a_g mode is represented by a damped oscillator $f_3(t)$ with the frequency of ω_3, initial phase of ϕ_3, and decay time of τ_3 (Eq. (4)), which is driven by the square of $E_{MIR}(t)$, $[E_{MIR}(t)]^2$. As a result, the high-frequency oscillation on the reflectivity change due to this mechanism is expressed by HPF$\{a_3{}^2[E_{MIR}(t)]^2 \otimes f_3(t)\}$. a_3 is the parameter determining the magnitude of this term, which has the same dimension as a_0 and a_1.

The red line in Fig. 4a shows the temporal profile of $[E_{MIR}(t)]^2$. $\Delta R_{HF}(t)/R$ for $E_{MIR} = 6.1$ MV cm^{-1} in Fig. 4b (the open circles) is well reproduced using Eqs. (1–5) as shown by the red line in Fig. 4b (see Supplementary Note 3 for the experimental and fitting curves in the wider temporal region). Each term in Eq. (1) is shown in the lower part. The used parameter values in this fitting are listed in Table 1. The obtained frequency values, ω_1 and ω_3, for oscillators $f_1(t)$ and $f_3(t)$ are 1184 cm^{-1} and 2211 cm^{-1}, which are almost in agreement with the frequencies of IR-active a_g mode (mode 1), $\Omega_1 = 1178$ cm^{-1}, and Raman-active a_g mode, $\Omega_{Raman} = 2207$ cm^{-1}, respectively. The latter is assigned to the a_g mode of the CN-stretching vibrations in TCNQ molecules[50]. The decay time τ_1 (1405 fs) of mode 1 is considerably shorter than the decay time τ_3 (4863 fs) of the Raman-active CN-stretching mode. It is probably because mode 1 is coupled to intermolecular charge transfers via the EMV coupling, but the Raman-active CN-stretching mode is not. $F(t)$ in Eq. (2) generates spin-density oscillation as well as charge-density one within each dimer and possibly decreases the spin-Peierls dimerization, which would be reflected in the low-frequency component below 10 THz, $\Delta R_{LF}(t)/R$, as mentioned earlier. In fact, as shown in Fig. 3g, maximum reflectivity change, max$|\Delta R_{LF}(t)/R|$, is proportional to $(E_{MIR})^2$ similarly to the $2\Omega_1$-oscillation amplitude A_{HF} (Fig. 3f).

Now, we explain the analysis of the low-frequency oscillations and discuss the feature of the destabilization of the spin-Peierls phase and reduction of dimeric molecular displacements extracted from the analysis. The time characteristic of $\Delta R_{LF}(t)/R$ ($E_{MIR} = 6.1$ MV cm^{-1}) and its Fourier power spectrum are represented using open circles in Fig. 4c and Fig. 5a, respectively. In Fig. 5a, two oscillations A and B with the frequencies of $\sim$150 cm^{-1} and $\sim$110 cm^{-1}, respectively, are observed. For comparison, the polarized Raman spectrum is shown in Fig. 5c. Oscillation A does not correspond to any Raman modes but is ascribed to the differential-frequency generation of two high-frequency oscillations, modes 1 and 2, with a frequency of $\Omega_2 - \Omega_1 = 152$ cm^{-1}. Oscillation B is attributed to the Raman mode represented by the solid triangle. Density functional theory (DFT) calculations revealed that the mode with 113.5 cm^{-1} was associated with dimerization, as illustrated in the upper part in Fig. 5d (see Supplementary Note 4 for the details of DFT calculations). These results suggest that the modulation of the spin density by the MIR pulse excitation reduces the dimeric molecular displacements, which drive oscillation B via the displacive excitation of coherent phonon mechanism[51]. This also suggests that the decrease in reflectivity, that is, the background component in $\Delta R_{LF}(t)/R$ is owing to a reduction in the average dimeric molecular displacements.

Table 1 Fitting parameters in Eqs. (2–4) used in the analysis of the time characteristic of the high-frequency components $\Delta R_{HF}(t)/R$.

$a_0 = 2.13 \times 10^{-2}$ MV^{-1} cm			
$a_1 = 4.08 \times 10^{-4}$ MV^{-1} cm	$\tau_1 = 1405$ fs	$\omega_1 = 1184$ cm^{-1}	$\phi_1 = -1.11$ rad
$a_3 = 9.15 \times 10^{-4}$ MV^{-1} cm	$\tau_3 = 4863$ fs	$\omega_3 = 2211$ cm^{-1}	$\phi_3 = 0.27$ rad
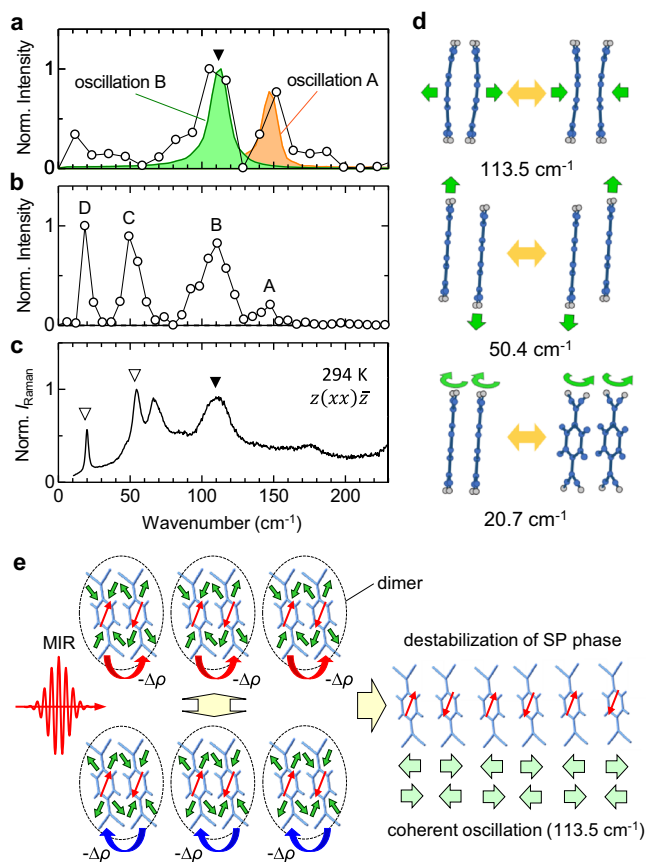
Fig. 5 Low-frequency oscillatory components driven by destabilization of the spin-Peierls phase. a Fourier power spectrum of the oscillatory component of the time characteristic of the low-frequency component $\Delta R_{LF}(t)/R$ (open circles). The orange and green solid lines show the Fourier power spectra of oscillation A and B obtained by the fitting procedure, respectively. **b** Fourier power spectrum of the oscillatory component of time characteristic of the reflectivity change $\Delta R(t)/R$ at 0.71 eV. **c** Raman spectrum, I_{Raman}, for $z(xx)\bar{z}$ configuration at 294 K. **d** Schematic of the molecular vibrations with ~113.5, 50.4, and 20.7 cm^{-1} obtained by the density functional theory (DFT) calculation. **e** Schematic of destabilization of the spin-Peierls (SP) phase by charge and spin density modulations induced by a mid-infrared (MIR) pulse. $\Delta\rho$ represents partial charge transfers. Green arrows show the coherent oscillation associated with the release of the dimerization (~113.5 cm^{-1}).

To confirm this interpretation, we performed a fitting analysis of $\Delta R_{LF}(t)/R$ using the following equations Eqs. (6), (7).

$$\frac{\Delta R_{LF}(t)}{R} = \text{LPF}\Big\{ b_0[F(t)] + b_1\big[F(t) \otimes f_4(t)\big] \tag{6}$$
$$+ b_2\big[E_{MIR}(t) \otimes f_1(t)\big]\big[E_{MIR}(t) \otimes f_2(t)\big] \Big\}$$

$$f_i(t) = \exp\left(-\frac{t}{\tau_i}\right)\sin\left(\omega_i t + \phi_i\right) \quad (i = 1, 2, 4) \tag{7}$$

LPF in Eq. (6) shows an operator that extracts a low-frequency component. $F(t)$ represents the total charge modulations within each dimer by the MIR electric field as expressed in Eq. (2) and is the driving force for the release of the dimerization. The first term in Eq. (6) shows the averaged decrease in the dimeric molecular displacements. This term is considered to depend on the amplitude of the charge modulation and therefore proportional to the envelope of HPF{$F(t)$}, which can be expressed by LPF[$F(t)$]. The second term in Eq. (6) represents the coherent

oscillation of the dimeric mode (oscillation B), which is also driven by LPF[$F(t)$]. Assuming that this dimeric mode is expressed by the damped oscillator, $f_4(t)$, in Eq. (7), this oscillation can be expressed by {LPF[$F(t)$]} $\otimes f_4(t)$, which is equal to LPF[$F(t) \otimes f_4(t)$]. The third term in Eq. (6) represents oscillation A, which is the beating produced by the differential frequency of two a_g-mode vibrations, mode 1 and 2. This component should be proportional to LPF{$[E_{MIR}(t) \otimes f_1(t)]$ $[E_{MIR}(t) \otimes f_2(t)]$}. b_0, b_1, and b_2 in Eq. (6) are the parameter determining the magnitude of each term.

Using Eqs. (6, 7), the time characteristic of $\Delta R_{LF}(t)/R$ experimentally obtained in Fig. 4c (the open circles) was almost reproduced as shown by the red line in the same figure. Three components in Eq. (6), are shown in the lower part. The used parameter values in this fitting are listed in Table 2. In this fitting procedure, the parameter values of the damped oscillator $f_1(t)$ are set to the same as those listed in Table 1 determined by the fitting analysis of $\Delta R_{HF}(t)/R$, except for the decay time τ_1 in the $[E_{MIR}(t) \otimes f_1(t)]^2$ term of $F(t)$ in Eq. (6). In general, the decay time of a coherent oscillation, τ, estimated from reflectivity changes is affected by two factors: the decay time of actual amplitude of the vibration, τ_0, and the decoherence of the oscillation. Because of the latter factor, the relation of $\tau_0 > \tau$ is expected. In our case, it is reasonable to consider that the suppression of the dimerization is determined not by τ including the effect of the decoherence but by the decay time of actual amplitude of the vibration, τ_0. Therefore, we set the decay time of oscillator $f_1(t)$ in the $[E_{MIR}(t) \otimes f_1(t)]^2$ term of $F(t)$ in Eq. (2) as a fitting parameter, τ_0. On the other hand, the decay time of oscillator $f_1(t)$ in the LPF{$[E_{MIR}(t) \otimes f_1(t)][E_{MIR}(t) \otimes f_2(t)]$} term should be equal to τ_1 since the oscillation from this term, that is, oscillation A should include the effect of the decoherence of high-frequency oscillations due to oscillators $f_1(t)$ and $f_2(t)$. τ_0 obtained by the fitting analysis of $\Delta R_{LF}(t)/R$ is 2500 fs, which is longer than $\tau_1 = 1405$ fs in Table 1 as expected.

The Fourier power spectra of the second and third terms in Eq. (6) are represented by the colored solid lines and shades in Fig. 5a, which almost reproduce the Fourier power spectra of $\Delta R_{LF}(t)/R$ (open circles). The frequency ω_4 of oscillation B is 112 cm^{-1}, which is in good agreement with the calculated frequency (113.5 cm^{-1}) of the dimerization mode shown in the upper part of Fig. 5d. The success of the fitting of the long-lived decrease in $\Delta R_{LF}(t)/R$ (the red line in Fig. 4c) with LPF{$b_0[F(t)]$} (the blue line in the same figure) demonstrates that the square of the total charge modulation expressed by $F(t)$, gives rise to the destabilization of the spin-Peierls phase. This result also excludes the possibility that the decrease in the dimeric molecular displacements is caused by a heating effect. In addition, the time characteristic of oscillation B shown by the green curve in Fig. 4c is of a cosine-type, indicating the displacive excitation of coherent phonon mechanism of its generation as pointed out above. This fact supports the validity of our interpretation again. Thus, we can conclude that the out-of-phase ag mode vibration excited by the MIR pulse destabilize the spin-Peierls phase.

The mechanism of destabilization of the spin-Peierls phase by MIR pulse excitation can be explained using a concept of Floquet states as follows. As suggested in the introduction, the resonant excitation of the IR-active a_g mode using an MIR pulse leads to a partial charge transfer, $\Delta\rho$, within each dimer synchronized with the a_g mode (left part of Fig. 5e). These processes hybridize the nonmagnetic dimer states expressed by $|{\uparrow}{\downarrow}, 00\rangle$, $|00, {\uparrow}{\downarrow}\rangle$ with the original singlet-dimer state expressed by $|{\uparrow}0, 0{\downarrow}\rangle$. In these expressions, the left (right) part shows the electron spin in the left (right) molecule, and the up-spin, down-spin, and spinless states are represented as ${\uparrow}0$, $0{\downarrow}$, and 00, respectively. This hybridized

Table 2 Fitting parameters in Eqs. (6, 7) used in the analysis of the time characteristic of the low-frequency components $\Delta R_{LF}(t)/R$.

$b_0 = -1.82$			
$b_1 = -2.41 \times 10^{-3}$	$\tau_4 = 756$ fs	$\omega_4 = 112$ cm^{-1}	$\phi_4 = 1.45$ rad
$b_2 = -3.84 \times 10^{-7}$ MV^{-2} cm^2	$\tau_2 = 3456$ fs	$\omega_2 = 1332$ cm^{-1}	$\phi_2 = -0.532$ rad

state is a type of Floquet state. In the nonmagnetic states $|\uparrow\downarrow, 00\rangle$ and $|00, \uparrow\downarrow\rangle$, the spin-Peierls mechanism does not work, so dimeric molecular displacements should decrease and oscillate coherently (the right part of Fig. 5e). The degree of hybridization, i.e., the coefficients of $|\uparrow\downarrow, 00\rangle$ and $|00, \uparrow\downarrow\rangle$ in the wavefunction of the vibrationally excited Floquet states are proportional to $\Delta\rho$ ($\propto E_{MIR}$), and the density of the nonmagnetic states is proportional to $(\Delta\rho)^2$. The descriptions of this formalism are reported in Supplementary Note 5. In the experiments, max$|\Delta R_{LF}(t)/R|$ represented the decrease in dimerization and was proportional to $(E_{MIR})^2$ as shown in Fig. 3g. The Floquet state produced by such periodic modulation of the spin density should be maintained as long as the intramolecular vibration, that is, the high-frequency oscillation (mode 1) persists in a coherent manner. As seen in Supplementary Fig. 3, the coherent intramolecular vibration continues up to at least 1.5 ps. This is the reason why the decrease in dimerization reflected by the decrease of the reflectivity (the negative background component in $\Delta R_{LF}(t)/R$) was sustained for up to a few picoseconds as seen in Fig. 4c.

MIR pump near-infrared reflectivity probe measurements on the Mott-gap transition band. To obtain more detailed information about the melting of the spin-Peierls phase, we measured the reflectivity change of the Mott-gap transition, using the same MIR-pulse excitation. The Mott-gap transition shows the peak structure at ~1 eV in the reflectivity spectrum in Figs. 2a and 6d, which is known to redshift with the decrease in dimerization[8,46]. Therefore, from the analysis of the transient reflectivity change of this peak, we will be able to evaluate quantitatively the decrease in dimerization. Figure 6a illustrates a schematic of the MIR pump near-IR probe reflection spectroscopy. This was not a subcycle measurement because we used near-IR probe pulses with a temporal width of ~90 fs. Figure 6b shows the time characteristic of $\Delta R(t)/R$ at 0.71 eV for an excitation by an MIR pulse with the central frequency of 1060 cm^{-1} and $E_{MIR} = 6.0$ MV cm^{-1}, which are almost the same as those used in the subcycle measurements. Around the time origin, a pulsed response appears in $\Delta R(t)/R$. Given that the magnitude of $\Delta R(0)/R$ is proportional to $(E_{MIR})^2$ (not shown), it is ascribed to the effect of the direct charge modulation, as expressed by the first term in Eq. (1). $\Delta R(t)/R$ at $t > 0.15$ ps exhibits coherent oscillations and a long-lived positive component, which resembles $\Delta R_{LF}(t)/R$ (Fig. 4c).

First, we discuss the oscillatory component $\Delta R_{OSC}(t)/R$ extracted from $\Delta R(t)/R$ at 0.71 eV, which is shown by the open circles in Fig. 6c. Fourier power spectrum of $\Delta R_{OSC}(t)/R$ is presented in Fig. 5b, in which four modes are identified. The higher two oscillations at ~150 cm^{-1} and 110 cm^{-1} correspond well to oscillations A and B observed in $\Delta R(t)/R$ by the visible probe measurement shown in Fig. 5a, respectively. We labeled the two lower-frequency oscillations at ~50 cm^{-1} and 20 cm^{-1} as C and D, respectively. To determine the frequencies of these oscillatory components more quantitatively, we analyzed the time characteristic of $\Delta R_{OSC}(t)/R$ in the temporal region from 0.5 ps to

5.5 ps using the following formula.

$$\frac{\Delta R_{OSC}(t)}{R} = \sum_{i=B,C,D} C_i \left[h(t) \otimes f_i(t) \right] \quad (8)$$

$$f_i(t) = \exp\left(-\frac{t}{\tau_i}\right) \sin\left(\omega_i t + \phi_i\right) \quad (i = B, C, D) \quad (9)$$

In the MIR pump near-IR probe measurements, the temporal widths of pump and probe pulses are both 90 fs, and the time resolution is estimated to be 127 fs. $h(t)$ in Eq. (8) is a response function in the measurement system and is expressed by a Gaussian profile of $\exp[-(t/76.4 \text{ fs})^2]$, the full width half maximum of which is equal to 127 fs. We assumed three damped oscillations ($i = B$, C, and D) for the oscillations and neglected the weak oscillation A. τ_i, ω_i, and ϕ_i are the decay time, frequency, and initial phase of each oscillation, respectively.

By the fitting procedure, the time characteristic of $\Delta R_{OSC}(t)/R$ was well reproduced as shown by the red line in Fig. 6c. Each oscillatory component is shown in the lower part. The used parameter values in this fitting are listed in Table 3. Frequencies of oscillations B, C, and D are 110 cm^{-1}, 49.3 cm^{-1}, and 20.3 cm^{-1}, respectively. According to the DFT calculation, the mode with 50.4 cm^{-1} is a shear-type mode, in which molecules are displaced parallel to the molecular plane as shown in the middle part in Fig. 5d. The mode with 20.7 cm^{-1} is another dimerization mode in which molecules rotate around the long axis of TCNQ$^-$ as illustrated in the bottom part in the same figure. Since those modes are also related to the dimerization, they can be interpreted as driven by the release of the dimerization. In fact, the magnitudes of the initial phases of those oscillations, ϕ_B, ϕ_C, and ϕ_D, are almost equal to $\pi/2$ or $-\pi/2$ rad, suggesting that those oscillations are also of the cosine type similarly to the coherent oscillation B due to mode 1. These oscillations are not observed in $\Delta R_{LF}(t)/R$ obtained by the visible probe measurements because their intensities are weak.

Here, we analyze the spectral changes of the Mott-gap transition and evaluate quantitatively the decrease in dimerization. We plotted in Fig. 6d the $\Delta R(t)$ spectra at $t = 1$ps, 2 ps, and 5 ps after the pulsed response disappeared together with the original R spectrum (the black solid line). $\Delta R(t)$ is negative above 0.85 eV and positive below this value. To analyze these spectra, we assumed that the original R spectrum consisted of two Lorentz oscillators, as previously reported[44], and changed the energy and intensity of the lower oscillator corresponding to the Mott-gap transition to reproduce the $\Delta R(t)$ spectra. Assuming a redshift and an intensity decrease of the Mott-gap transition, the $\Delta R(t)$ spectra are approximately reproduced, as shown by the red broken line in Fig. 6d. From the magnitude of the redshift, the decrease in dimeric molecular displacements was estimated to be ~10% of the original magnitude. The decrease in the Mott-gap transition intensity was attributed to the decrease in the intradimer transfer integrals. Details of the analysis of the $\Delta R(t)$ spectra are provided in Supplementary Note 6.

Finally, we compare the destabilization of the spin-Peierls phase in K-TCNQ by the vibrational excitation studied here with that by the electronic excitation beyond the gap using a 1.55-eV
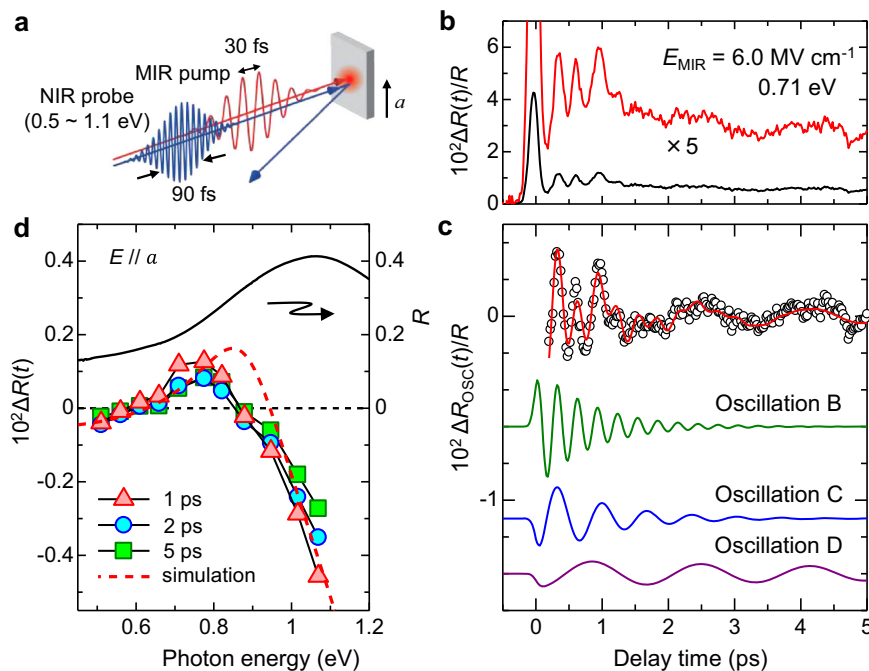
Fig. 6 Reflectivity changes in the Mott-gap transition band in the near-infrared (NIR) region induced by the mid-infrared (MIR)-pump pulse.
a Schematic of the experimental setup. **b** Time characteristic of the reflectivity (R) change $\Delta R(t)/R$ at 0.71 eV at 294 K for the MIR pulse with the maximum electric-field amplitude, E_{MIR}, of 6.0 MV cm^{-1} (the black solid line). The red solid line represents five times $\Delta R(t)/R$. **c** Time characteristic of the oscillatory component, $\Delta R_{OSC}(t)/R$, (open circles). The red line shows the fitting curve. Time characteristics of oscillatory components B, C, and D determined by the fitting procedure are shown by the green, blue, and purple solid lines, respectively. **d** The R spectrum for the electric field of light E parallel to the a axis ($E//a$) (the black solid line) due to the Mott-gap transition band and $\Delta R(t)$ spectra at the delay time of the probe pulse relative to the MIR-pump pulse, $t = 1$ ps, 2 ps, and 5 ps (the red triangles, the blue circles and green squares, respectively). The error bars are smaller than the sizes of data points. The red broken line shows the simulation curve.

Table 3 Fitting parameters in Eqs. (8, 9) used in the analysis of the time characteristic of the oscillatory component $\Delta R_{OSC}(t)/R$.

$C_B = 6.44 \times 10^{-3}$	$\tau_B = 780$ fs	$\omega_B = 110$ cm^{-1}	$\varphi_B = 1.15$ rad
$C_C = 2.71 \times 10^{-3}$	$\tau_C = 959$ fs	$\omega_C = 49.3$ cm^{-1}	$\varphi_C = -1.49$ rad
$C_D = 7.64 \times 10^{-4}$	$\tau_D = 7.15$ ps	$\omega_D = 20.3$ cm^{-1}	$\varphi_D = -1.70$ rad

pulse previously reported[8,46]. In the electronic excitation with the 1.55-eV pulse, it was revealed that the spin-Peierls phase became unstable by photogenerated spinless holons and doublons fragmenting the one-dimensional antiferromagnetic spin chains. This mechanism of destabilization of the spin-Peierls phase is essentially different from that by the charge-spin modulation by the MIR excitation reported here. It is therefore interesting to compare the efficiency of the decrease in the dimeric molecular displacements by the photoexcitation and MIR excitations. In fact, we evaluated the low-energy shift of the Mott gap transition from the change of the reflectivity spectrum due to the 1.55-eV excitation and estimated the magnitude of the decrease in the dimeric molecular displacements as in the case of MIR excitation. The results show that for the 1.55-eV excitation with the excitation photon density of 0.095 photon per TCNQ, the decrease in the dimeric molecular displacements is ~50%. Furthermore, for each of the 1.55-eV and MIR excitations, we evaluated the total amount of light energy absorbed in the region from the crystal surface to the penetration depth (148 nm) of the probe pulse at 0.775 eV, the reflectivity change at which characterizes the low-energy shift of Mott gap transition, and compared the decreases in the dimeric molecular displacements

per unit energy. The result revealed that the energy efficiency of the decrease in the dimeric molecular displacements was approximately three times higher for the MIR excitation than for the 1.55-eV excitation. This comparison demonstrates that the generation of the charge-spin modulated Floquet state by the MIR excitation is effective for the electronic state control. Supplementary Note 7 details the analysis of the reflectivity change by the 1.55-eV excitation and the comparison of the efficiency of the decrease in the dimeric molecular displacements by the MIR and 1.55-eV excitations.

Conclusion
In summary, we demonstrated that the spin-density modulation owing to the intermolecular charge transfer induced by the a_g-mode excitation caused destabilization of the spin-Peierls phase. This phase control using the periodic spin-density modulation can be regarded as a typical example of Floquet engineering. The MIR pump visible subcycle reflection probe and near-IR reflection probe measurements revealed that the time-periodic spin-density modulation by the a_g-mode excitation induced the hybridization of the nonmagnetic dimer states with the original singlet-dimer states and resulted in the destabilization of the spin-Peierls phase. The resultant decrease in dimerization was accompanied by the multiple coherent molecular oscillations corresponding to the release of dimeric molecular displacements. The coupling between intramolecular vibrations and electronic systems has been observed in many molecular solids. Therefore, by applying the method proposed here using electron and spin-density modulations induced by intramolecular vibrational excitations to other molecular solids, it may be possible to generate

charge-spin modulated Floquet states and drive various types of efficient phase transitions.

Methods

Sample preparations. Single crystals of K-TCNQ were grown from KI and TCNQ by the diffusion method[52]. A typical size of *ab* plane of used single crystals is 5 mm × 0.5 mm, on which reflection measurements are performed. Their typical thickness is 0.5 mm.

Steady-state optical spectroscopy measurements. The polarized reflectivity spectra were measured using a specially designed spectrometer with a 25-cm-grating monochromator in the visible and near-IR region (0.5-5.0 eV) and a Fourier-transform infrared spectrometer in the MIR region (0.08-1.2 eV). Both of these spectrometers were equipped with optical microscopes. The complex dielectric constant $\tilde{\varepsilon}(\omega)$ spectra were calculated from the R spectra using the Kramers–Kronig transformation. The polarized Raman spectra were measured by using a Raman spectrometer equipped with a He-Ne laser (1.96 eV) and an optical microscope. The obtained scattering intensities were corrected using a Bose factor.

MIR pump ultrashort visible reflectivity probe subcycle spectroscopy. The schematic diagram of the MIR pump ultrashort visible probe subcycle spectroscopy is reported in Supplementary Note 1. In this measurement, a Ti: sapphire regenerative amplifier with the central photon energy of 1.55 eV, temporal width of ~35 fs, maximum pulse energy of 7.5 mJ, and repetition rate of 1 kHz is used as a light source. From the output from the regenerative amplifier, two pulses with 4.0 mJ and 1.0 mJ are picked up. The former is introduced to a twin-optical parametric amplifier (OPA). In the twin-OPA, the pulse is further divided into two pulses, which are input to two OPAs, OPA1 and OPA2. A part of the pulse excites a sapphire plate to generate a white-light pulse, which is used as a seed pulse in OPA1 and OPA2 in common. The pulses input to OPA1 and OPA2 are used for the amplification of the seed pulse in each OPA. The near-IR idler pulses output from OPA1 and OPA2 are guided onto a 1-mm thick GaSe crystal, and an MIR pulse is generated from the GaSe crystal by a difference frequency generation (DFG) process[53]. The MIR pulse thus obtained is divided into two pulses. One is used for a pump pulse to excite a sample and the other is used to measure electric-field waveform of the pulse itself during the measurement of transient reflectivity changes of the sample. To stabilize the carrier envelope phase of the MIR pulse, the feedback control of the optical path length through OPA2 is performed so that two optical path lengths through OPA1 and OPA2 are equal. In addition, another feedback control is performed using the delay line of the probe pulse so that the optical path length difference of the pump and probe pulses are unchanged with time[54]. The other output from the regenerative amplifier is input to a home-made noncollinear OPA (NOPA) to generate ultrashort visible pulses[55]. A typical spectrum of an output pulse from NOPA is shown in the blue shade in Fig. 2a, the central photon energy of which is 2.0 eV. The temporal width of the pulse was evaluated using a frequency-resolved optical gating (FROG) method[56].

A part of the pulse is used as a sampling pulse for an electro-optical sampling to measure the electric-field waveform of the MIR pulse. In the electro-optical sampling, LiGaS$_2$ with the thickness of 20μm is used as a nonlinear optical crystal to give rise to a polarization rotation of the sampling pulse proportional to the MIR electric field. A typical electric-field waveform and its Fourier power spectrum of the MIR pulse are shown in Fig. 3a and Fig. 2a (the red shade), respectively. The magnitude of the electric-field amplitude is calculated from the electric-field

waveform, $E_{MIR}(t)$, the beam diameter, and the fluence of the MIR pulse[57].

MIR-pump near-IR reflectivity probe spectroscopy. In the MIR pump near-IR probe reflection spectroscopy, another regenerative amplifier with the central photon energy of 1.55 eV, temporal width of ~90 fs, maximum pulse energy of 4.7 mJ, and repetition rate of 1 kHz is used as the light source (see Supplementary Note 1). From the output of the regenerative amplifier, two pulses with 1.8 mJ and 0.7 mJ are input to OPA3 and OPA4, respectively. An MIR pump pulse is generated from the signal and idler pulses output from OPA3 via the DFG process in GaSe. This MIR pulse is tuned to have the same spectrum as that used for the subcycle spectroscopy measurement. Near-IR probe pulses with the photon energy of 0.5 eV-1.1 eV are generated from OPA4. These near-IR pulses have temporal widths of ~90 fs. Therefore, this is a non-subcycle measurement.

References

1. Nasu, K. *Photoinduced Phase Transitions* (World Scientific, 2004).
2. Zhang, J. & Averitt, R. D. Dynamics and control in complex transition metal oxides. *Annu. Rev. Mater. Res.* **44**, 19–43 (2014).
3. Giannetti, C. et al. Ultrafast optical spectroscopy of strongly correlated materials and high-temperature superconductors: a non-equilibrium approach. *Adv. Phys.* **65**, 58–238 (2016).
4. Fiebig, M., Miyano, K., Tomioka, Y. & Tokura, Y. Visualization of the local insulator-metal transition in Pr$_{0.7}$Ca$_{0.3}$MnO$_3$. *Science* **280**, 1925–1928 (1998).
5. Cavalleri, A. et al. Femtosecond structural dynamics in VO$_2$ during an ultrafast solid-solid phase transition. *Phys. Rev. Lett.* **87**, 237401 (2001).
6. Iwai, S. et al. Ultrafast optical switching to a metallic state by photoinduced Mott transition in a halogen-bridged nickel-chain compound. *Phys. Rev. Lett.* **91**, 057401 (2003).
7. Chollet, M. et al. Gigantic photoresponse in ¼-filled-band organic salt (EDO-TTF)$_2$PF$_6$. *Science* **307**, 86–89 (2005).
8. Okamoto, H. et al. Ultrafast photoinduced melting of a spin-peierls phase in an organic charge-transfer compound, K-tetracyanoquinodimethane. *Phys. Rev. Lett.* **96**, 037405 (2006).
9. Perfetti, L. et al. Time evolution of the electronic structure of 1*T*-TaS$_2$ through the insulator-metal transition. *Phys. Rev. Lett.* **97**, 067402 (2006).
10. Kübler, C. et al. Coherent structural dynamics and electronic correlations during an ultrafast insulator-to-metal phase transition in VO$_2$. *Phys. Rev. Lett.* **99**, 116401 (2007).
11. Matsubara, M. et al. Ultrafast photoinduced insulator-ferromagnet transition in the perovskite manganite Gd$_{0.55}$Sr$_{0.45}$MnO$_3$. *Phys. Rev. Lett.* **99**, 207401 (2007).
12. Baum, P., Yang, D.-S. & Zewail, A. H. 4D visualization of transitional structures in phase transformations by electron diffraction. *Science* **318**, 788–792 (2007).
13. Polli, D. et al. A coherent orbital waves in the photo-induced insulator–metal dynamics of a magnetoresistive manganite. *Nat. Mater.* **6**, 643–647 (2007).
14. Schmitt, F. et al. Transient electronic structure and melting of a charge density wave in TbTe$_3$. *Science* **321**, 1649–1652 (2008).
15. Eichberger, M. et al. Snapshots of cooperative atomic motions in the optical suppression of charge density waves. *Nature* **468**, 799–802 (2010).
16. Okamoto, H. et al. Photoinduced transition from Mott insulator to metal in the undoped cuprates Nd$_2$CuO$_4$ and La$_2$CuO$_4$. *Phys. Rev. B* **83**, 125102 (2011).
17. Stojchevska, L. et al. Ultrafast switching to a stable hidden quantum state in an electronic crystal. *Science* **344**, 177–180 (2014).

18. Fausti, D. et al. Light-induced superconductivity in a stripe-ordered cuprate. *Science* **331**, 189–191 (2011).
19. Kaiser, S. et al. Optical properties of a vibrationally modulated solid state Mott insulator. *Sci. Rep.* **4**, 3823 (2014).
20. Singla, R. et al. THz-frequency modulation of the Hubbard U in an organic Mott insulator. *Phys. Rev. Lett.* **115**, 187401 (2015).
21. Mitrano, M. et al. Possible light-induced superconductivity in K_3C_{60} at high temperature. *Nature* **530**, 461–464 (2016).
22. Mankowsky, R., von Hoegen, A., Först, M. & Cavalleri, A. Ultrafast reversal of the ferroelectric polarization. *Phys. Rev. Lett.* **118**, 197601 (2017).
23. Maehrlein, S., Paarmann, A., Wolf, M. & Kampfrath, T. Terahertz sum-frequency excitation of a raman-active phonon. *Phys. Rev. Lett.* **119**, 127402 (2017).
24. von Hoegen, A., Mankowsky, R., Fechner, M., Först, M. & Cavalleri, A. Probing the interatomic potential of solids with strong-field nonlinear phononics. *Nature* **555**, 79–82 (2018).
25. Schmidt, C. et al. Signatures of transient Wannier-Stark localization in bulk gallium arsenide. *Nat. Commun.* **9**, 2890 (2018).
26. Umanodan, T. et al. Ultrafast control of ferroelectricity with dynamical repositioning of protons in a supramolecular cocrystal studied by femtosecond nonlinear spectroscopy. *J. Phys. Soc. Jpn.* **88**, 013705 (2019).
27. Morimoto, T. et al. Ionic to neutral conversion induced by resonant excitation of molecular vibrations coupled to intermolecular charge transfer. *Phys. Rev. Res.* **3**, L042028 (2021).
28. Sono, N. et al. Phonon-dressed states in an organic Mott insulator. *Commun. Phys.* **5**, 72 (2022).
29. Yamakawa, T., Miyamoto, T., Sakai, D. & Okamoto, H. Dynamical aspects of excitonic Floquet states generated by a phase locked mid-infrared pulse in a one-dimensional Mott insulator. *N. J. Phys.* **25**, 093044 (2023).
30. Liu, M. et al. Terahertz-field-induced insulator-to-metal transition in vanadium dioxide metamaterial. *Nature* **487**, 345–348 (2012).
31. Mayer, B. et al. Tunneling breakdown of a strongly correlated insulating state in VO_2 induced by intense multiterahertz excitation. *Phys. Rev. B* **91**, 235113 (2015).
32. Wang, Y. H., Steinberg, H., Jarillo-Herrero, P. & Gedik, N. Observation of Floquet-Bloch states on the surface of a topological insulator. *Science* **342**, 453–457 (2013).
33. Aoki, H. et al. Nonequilibrium dynamical mean-field theory and its applications. *Rev. Mod. Phys.* **86**, 779–837 (2014).
34. Mahmood, F. et al. Selective scattering between Floquet-Bloch and Volkov states in a topological insulator. *Nat. Phys.* **12**, 306–310 (2016).
35. Oka, T. & Kitamura, S. Floquet engineering of quantum materials. *Annu. Rev. Condens. Mater. Phys.* **10**, 387–408 (2019).
36. Giovannini, U. D. & Hübener, H. Floquet analysis of excitations in materials. *J. Phys. Mater.* **3**, 012001 (2020).
37. McIver, J. W. et al. Light-induced anomalous Hall effect in graphene. *Nat. Phys.* **16**, 38–41 (2020).
38. Rudner, M. S. & Lindner, N. H. Band structure engineering and non-equilibrium dynamics in Floquet topological insulators. *Nat. Rev. Phys.* **2**, 229–244 (2020).
39. Aeschlimann, S. et al. Survival of Floquet-Bloch states in the presence of scattering. *Nano Lett.* **21**, 5028–5035 (2021).
40. Painelli, A. & Girlando, A. Electron-molecular vibration (e-mv) coupling in charge-transfer compounds and its consequences on the optical spectra: a theoretical framework. *J. Chem. Phys.* **84**, 5655–5671 (1986).
41. Konno, M., Ishii, T. & Saito, Y. The crystal structures of the low- and high-temperature modifications of Potassium 7,7,8,8-Tetraeyanoquinodimethanide. *Acta. Cryst. B* **33**, 763–770 (1977).
42. Lépin, Y., Caillé, A. & Larochelle, V. Potassium-tetracyanoquinodimethane (K-TCNQ): a spin-Peierls system. *Phys. Rev. B* **18**, 3585–3592 (1978).
43. Yakushi, K., Kusaka, T. & Kuroda, H. Low-temperature reflection spectrum of K-TCNQ single crystal. *Chem. Phys. Lett.* **68**, 139–142 (1979).
44. Okamoto, H., Tokura, Y. & Koda, T. Optical study of structural phase transition in organic charge-transfer crystals K- and Rb-tetracyanoquinodimethane. *Phys. Rev. B* **36**, 3858–3867 (1987).
45. Bray, J. W., Interrante, L. V., Jacobs, I. S. & Miller, J. S. In *Extended Linear Chain Compounds* 3rd edn Vol. 2 (ed Miller, J. S.) Ch. 353–415 (Plenum Press, 1983).
46. Ikegami, K. et al. Ultrafast photoinduced melting of spin-Peierls phase in the organic charge-transfer compounds alkali-tetracyanoquinodimethane. *Phys. Rev. B* **76**, 085106 (2007).
47. Tanner, D. B., Jacobsen, C. S., Bright, A. A. & Heeger, A. J. Infrared studies of the energy gap and electron-phonon interaction in potassium-tetracyanoquinodimethane (K-TCNQ). *Phys. Rev. B* **16**, 3283–3290 (1977).
48. Painelli, A., Girlando, A. & Pecile, C. Accurate electron-molecular vibration coupling constants from powders optical spectra: TCNQ and TTF. *Solid State Commun.* **52**, 801–806 (1984).
49. Khvostenko, O. G., Kinzyabulatov, R. R., Khatymova, L. Z. & Tseplin, E. E. The lowest triplet of Tetracyanoquinodimethane via UV-vis absorption spectroscopy with Br-containing solvents. *J. Phys. Chem. A* **121**, 7349–7355 (2017).
50. Truong, K. D. & Carlone, C. Raman spectrum of potassium tetracyanoquinodime thane crystals. *Phys. Rev. B* **20**, 2238–2246 (1979).
51. Zeiger, H. J. et al. Theory for displacive excitation of coherent phonons. *Phys. Rev. B* **45**, 768–778 (1992).
52. Singh, Y., Goswami, D. P., Bala, M. & Kalra, M. L. Large needle-shaped highly conducting organic charge transfer complexes with asymmetric donor molecules. *J. Cryst. Growth* **123**, 601–604 (1992).
53. Sell, A., Leitenstorfer, A. & Huber, R. Phase-locked generation and field-resolved detection of widely tunable terahertz pulses with amplitudes exceeding 100 MV/cm. *Opt. Lett.* **33**, 2767–2769 (2008).
54. Yamakawa, T. et al. Long-term stabilization of carrier envelope phases of mid-infrared pulses for the precise detection of phase-sensitive responses to electromagnetic waves. *AIP Adv.* **10**, 025311 (2020).
55. Adachi, S., Watanabe, Y., Sudo, Y. & Suzuki, T. Few-cycle pulse generation from noncollinear optical parametric amplifier with static dispersion compensation. *Chem. Phys. Lett.* **683**, 7–11 (2017).
56. Trebino, R. et al. Measuring ultrashort laser pulses in the time-frequency domain using frequency-resolved optical gating. *Rev. Sci. Instrum.* **68**, 3277–3295 (1997).
57. Blanchard, F. G. et al. Improved terahertz two-color plasma sources pumped by high intensity laser beam. *Opt. Expr.* **17**, 6044–6052 (2009).

Acknowledgements

Author contributions

D.S., T.Y., H.U., R.I. and T.M performed experiments. D.S., T.Y. and T.M. analysed the experimental data. H.O prepared the sample and coordinated the study. The manuscript was written by D.S., T.M. and H.O. with inputs from all authors.

Competing interests

The authors declare no competing interests.

Additional information